Supplementary Material to Nonlinear axisymmetric Taylor-Couette flow in a dilute gas: multi-roll transition and the role of compressibility

Pratik Aghor[1] and Meheboob Alam [1]†

[1]Engineering Mechanics Unit, Jawaharlal Nehru Centre for Advanced Scientific Research, Jakkur P.O., Bangalore 560064, India

(Received xx; revised xx; accepted xx)

† Email address for correspondence: meheboob@jncasr.ac.in

Appendix A. Numerical method and the grid independence test

A.1. *Discretization and the numerical algorithm*

A variant of the explicit numerical scheme used by Harada (1980) is implemented to solve (2.6a–2.6e) and (2.8) in the main paper (Aghor & Alam 2021). In this method, the primitive variables are used to write down the finite difference approximation of the governing equations and the related boundary conditions on uniform, staggered grids in the meridional (r, z)-plane. The choice of staggered grid is motivated by the physics of the problem since we do not have boundary conditions for density and pressure. To avoid imposing artificial boundary conditions on ρ and p, the calculation of density and pressure fields is pushed inside the domain using staggered grid, see Harada (1980).

To approximate first-order spatial derivatives, the central difference method is used; the upwind scheme or the donor-cell method is adopted for convective derivatives. A second-order leapfrog-type DuFort-Frankel method is used for diffusion terms and time stepping, the details of which can be found in LeVeque (2007). For example, the second derivative of some physical quantity ψ is approximated as

$$\delta_x \delta_x \psi_j = \frac{1}{\Delta x_j}\left[\left(\psi_{(j+1)} - \bar{\psi_j}\right)/\Delta x_{j+\frac{1}{2}} - \left(\bar{\psi_j} - \psi_{(j-1)}\right)/\Delta x_{j-\frac{1}{2}}\right]^n, \tag{A 1}$$

where

$$\bar{\psi_j}^n = \frac{1}{2}\left(\psi_j^{n+1} - \psi_j^n\right), \tag{A 2a}$$

$$\Delta x_{j+\frac{1}{2}} = \frac{1}{2}\left(\Delta x_j + \Delta x_{j+1}\right), \tag{A 2b}$$

and

$$\Delta x_j = \frac{1}{2}\left(\Delta x_{j+\frac{1}{2}} + \Delta x_{j-\frac{1}{2}}\right). \tag{A 2c}$$

Note that $\Delta x_{j+\frac{1}{2}} = \Delta x_{j+\frac{1}{2}} = \Delta x_j$ for uniform grids. Equation (A 1) seems to represent an implicit scheme, since ψ_j^{n+1} appears on the right hand side of Eq. (A 1) via Eq. (A 2*a*); however, the term ψ_j^{n+1} from the future is brought back to the left hand side (in all discretized equations) to make the scheme explicit.

To avoid computational splitting inherent to the DuFort-Frankel method, the filtering is done after every $m = 20$ dimensionless time-steps, using the following formula,

$$\psi^{n\pm\frac{1}{2}} = \frac{1}{2}\left(\psi^n + \psi^{n\pm1}\right) \tag{A 3}$$

as suggested by Harada (1980) and Hyun & Park (1992).

The algorithm to obtain the numerical solution of discretized equations is summarized below:

(i) In the present numerical scheme, we need two initial conditions, one physical and other computational, in order to march in time. We take $\psi^1 = \psi^0$, where ψ can be $u, v, w, \bar{\rho}, T, p$.

(ii) Solve for $(\bar{\rho}u)^{n+1}$, $(\bar{\rho}v)^{n+1}$, $(\bar{\rho}w)^{n+1}$ from momentum equations (2.6b-2.6d).

(iii) Get $\bar{\rho}^{n+1}$ by plugging in the updated velocity fields obtained from the previous step into the continuity equation (2.6a).

(iv) Get $(\bar{\rho}T)^{n+1}$ from the energy equation (2.6e).

(v) Update pressure p^{n+1} from the equation of state.

(vi) Obtain $[u^{n+1}, v^{n+1}, w^{n+1}, T^{n+1}]$ by dividing $[(\bar{\rho}u)^{n+1}, (\bar{\rho}v)^{n+1}, (\bar{\rho}w)^{n+1}, (\bar{\rho}T)^{n+1}]$ by $\bar{\rho}^{n+1}$.

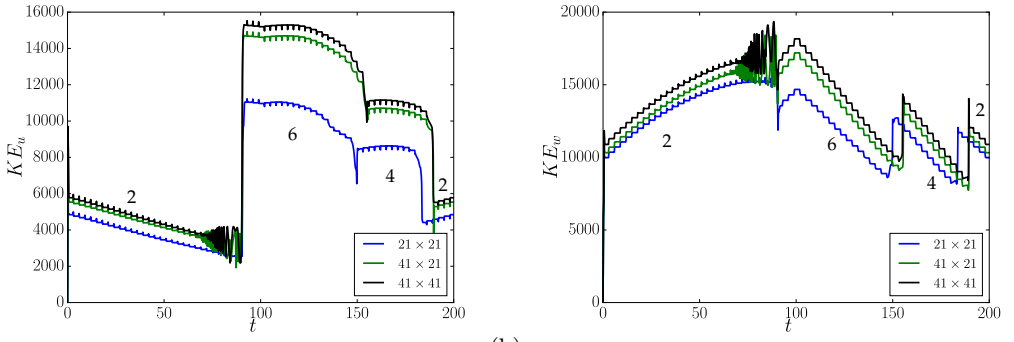

(a) (b)

FIGURE S.20. Dependence on grid-size of the time-evolution of (a) KE_u, Eq. (A 4), and (b) KE_w, Eq. (A 5); the numbers of grid-points along axial and radial directions ($N_z \times N_r$) are as follows: 21×21 (Black), 41×21 (Blue) and 41×41 (Green). The aspect-ratio Γ is increased from 3.1 to 6.4 and then decreased back to 3.1 in time; Γ was changed in steps of $d\Gamma = 0.1$ after every 6×10^5 time-steps, i.e. with a ramp rate of $d\Gamma/dt \approx 3.33 \times 10^{-2}$, where t is the dimensionless time. Parameter values are $Re = 200$, $Ma = 1$ and $Pr = 1$, with stationary outer cylinder.

(vii) To avoid computational splitting error caused by leap-frogging, filter after every m time steps according to (A 3).

(viii) Keep going until the steady state is reached.

We monitor the temporal evolution of the global kinetic energy [based on (i) azimuthal, (ii) axial and (iii) radial velocities, (A 4)] which saturates to a constant value when the steady state is reached.

A.2. *Grid independence test*

In order to check the grid dependency of present calculations, a set of runs was done with three different grid-sizes ($N_z \times N_r = 21 \times 21$, 41×21 and 41×41, where N_z and N_r denote the number of grids along axial and radial directions, respectively) at a Reynolds number of $Re = 200$ which represents the highest Re (see figure 5 in Aghor & Alam (2021)) accessed to study transitions among symmetric rolls. The temporal evolutions of global kinetic energies based on (i) the radial velocity,

$$KE_u = \left\langle \frac{1}{2}\rho u^2 \right\rangle_{(r,\theta,z)} = 2\pi \int_{\frac{\eta}{1-\eta}}^{\frac{1}{1-\eta}} \int_0^h (\rho u^2/2) r dr dz, \tag{A 4}$$

and (ii) the axial velocity,

$$KE_w = \left\langle \frac{1}{2}\rho w^2 \right\rangle_{(r,\theta,z)} = 2\pi \int_{\frac{\eta}{1-\eta}}^{\frac{1}{1-\eta}} \int_0^h (\rho w^2/2) r dr dz, \tag{A 5}$$

are shown in figures S.20(a) and S.20(b), respectively, for $Re = 200$ with other parameters as in figure 4(b) in the main paper (Aghor & Alam 2021). For each grid-size, the aspect-ratio Γ is increased from 3.1 to 6.4 and then decreased back to 3.1, with a ramp rate of $d\Gamma/dt = 0.0333$ where t is the dimensionless time (based on viscous time scale).

As clarified in §3.1 in the main paper (Aghor & Alam 2021), the jumps in kinetic energies in figure S.20(a,b) refer to sudden increase/decrease in the number of Taylor rolls. It is seen in figure S.20 that there are oscillations near the first transition [$2 \to 6$ rolls] during the up-sweep run – this can possibly be eradicated by using a smaller time-step and a longer waiting time before changing the aspect ratio (i.e. by reducing the

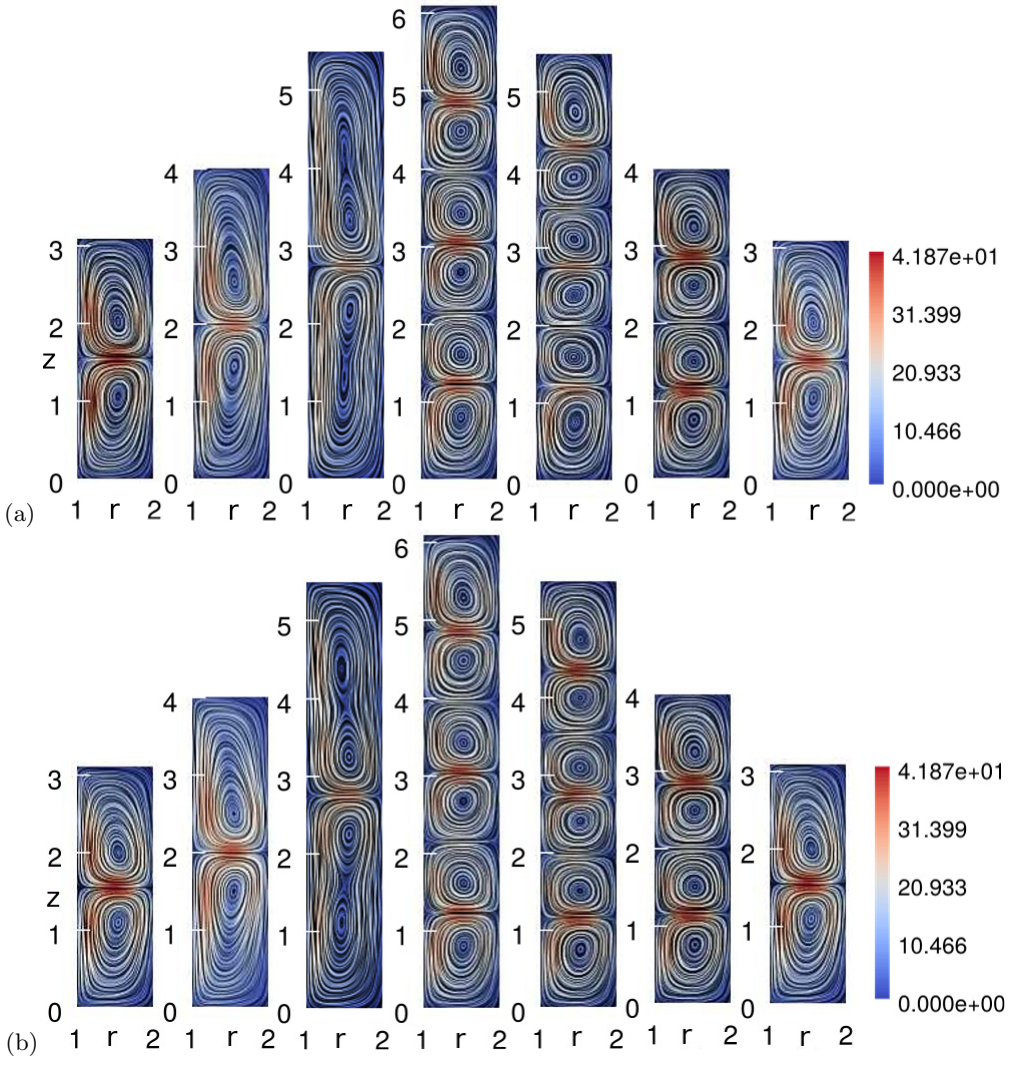

FIGURE S.21. Dependence of grid-size on streamline patterns in (r, z) plane – upper panels: 21×21; lower panels: 41×41. For both cases, Γ was increased from 3.1 to 6.4 and decreased back to 3.1 at a ramp rate of $d\Gamma/dt = 0.033$. Parameter values are the same as in figure S.20.

ramp rate $d\Gamma/dt$). The point to be noted is that a grid-size of $(N_z \times N_r) = (41 \times 21)$ is sufficient to accurately predict (i) the onset of roll-transitions (such as in the phase-diagram in figure 5) as well as (ii) the kinetic energy levels at an inner-cylinder Reynolds number of $Re = 200$.

Figure S.21(a,b) displays the snapshots of streamline patterns at different Γ during the above protocol of quasi-static change in Γ: while the upper panels refer to a grid-size of $(N_z \times N_r) = (21 \times 21)$, the lower panels correspond to a grid-size of $(N_z \times N_r) = (41 \times 41)$. The patterns look strikingly similar even with a coarser grid of $(N_z \times N_r) = (21 \times 21)$, but the velocity-levels are slightly over-predicted compared to those at $(N_z \times N_r) = (41 \times 41)$. Collectively, based on results presented in figures S.20 and S.21, we conclude that the phase diagram (viz. figure 5), the bifurcation diagrams (such as figures 4(c), 6(b), 8(a-c) and 10(a,b); Aghor & Alam (2021)) and the patterns of Taylor rolls and other hydrodynamic fields are grid-independent and hence robust.

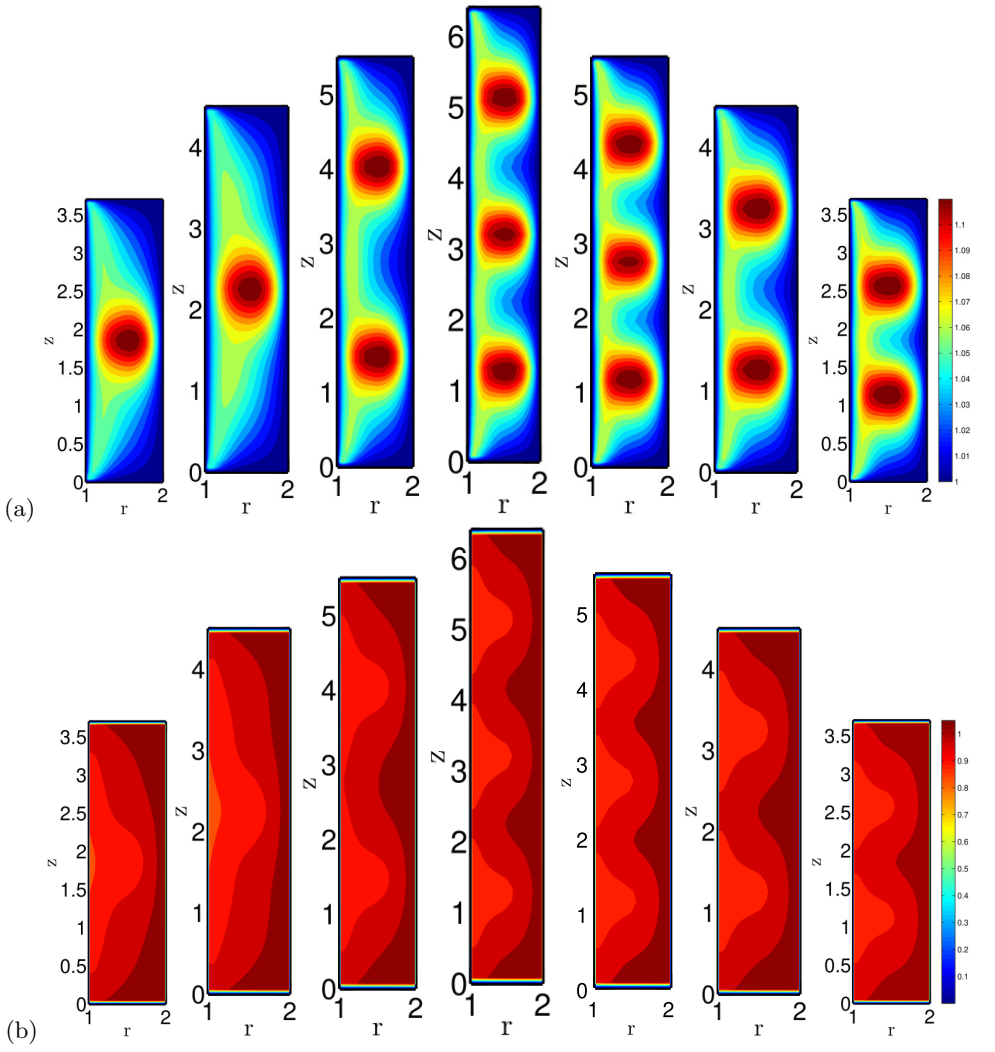

FIGURE S.22. (a) Color-map of temperature (upper panels) and (b) density (lower panels) in the (r, z) plane. Parameter values are as in figure 6(a) in Aghor & Alam (2021).

With reference to streamline plots in figure 6(a) in the main paper (Aghor & Alam 2021) that hold for $Re = 150$, the meridional-plane temperature $T(r, z)$ and density $\rho(r, z)$ are shown in figures S.22(a) and S.22(b), respectively. It is seen that the temperature maxima is located within the annular gap, whereas the density maxima is located near the outer cylinder; the red-colored blobs in each panel of figure S.22(a) refer to the locations of outward jets through which a relatively hotter and rarefied gas is transported from the inner towards the outer cylinder. The outward jets are also correlated with the local maxima of the azimuthal velocity field $v(r, z)$ and the specific angular momentum $\mathcal{L}(r, z) = \langle \rho v r \rangle$ as confirmed in figure S.23(a,b).

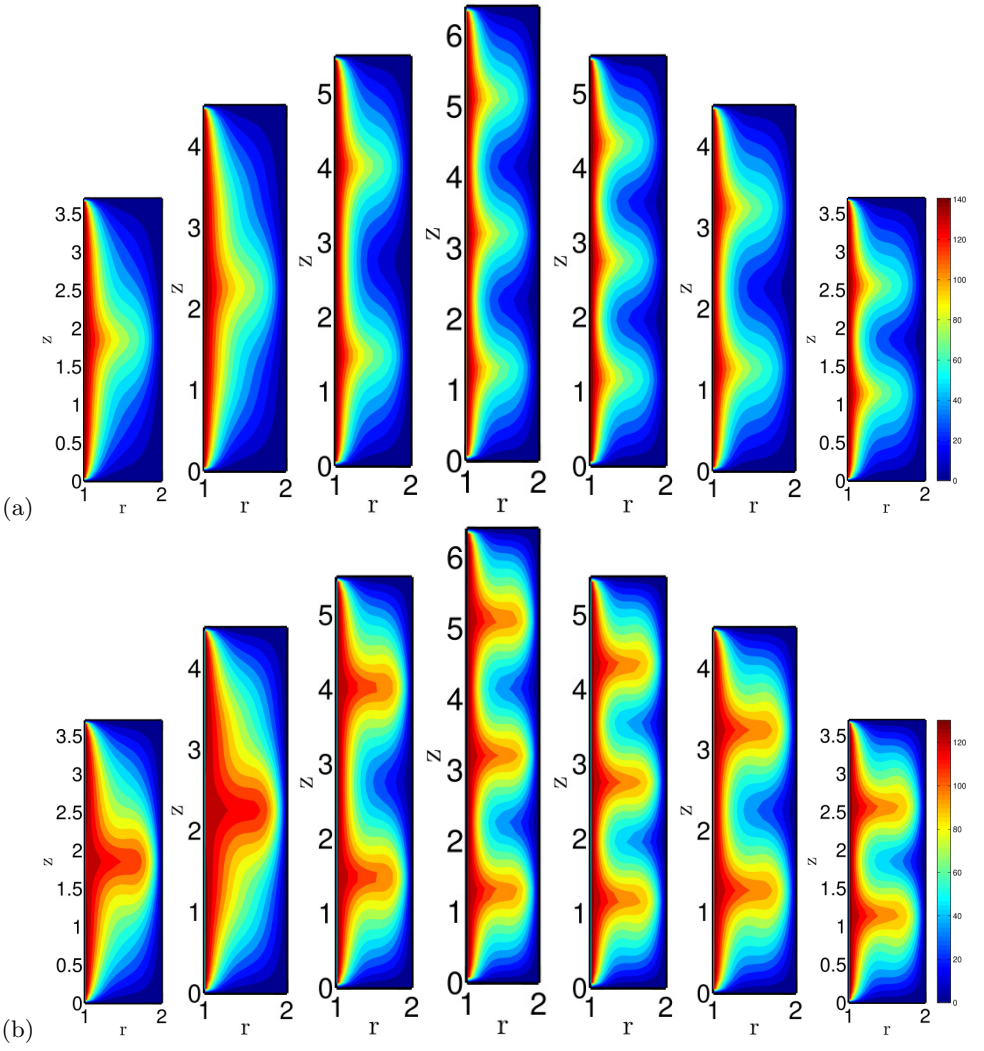

FIGURE S.23. Color-maps of (a) azimuthal velocity (upper panels) and (b) specific angular momentum (lower panels) in the (r, z) plane. Parameter values are as in figure 6(a) in Aghor & Alam (2021).

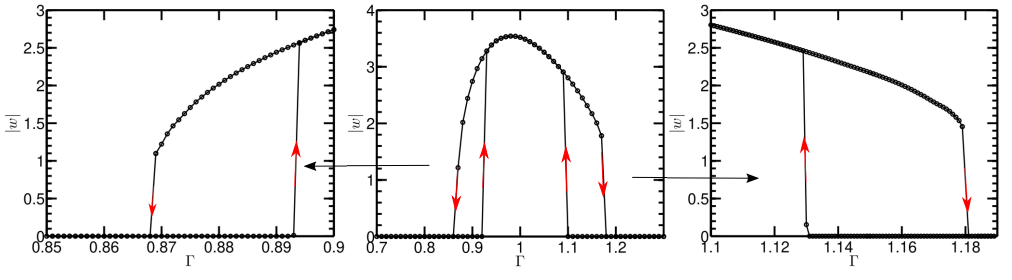

FIGURE S.24. Effect of ramp rate on hysteresis-regions at $Re = 180$, with the middle panel being the same as figure 17(a) in Aghor & Alam (2021), each panel representing bifurcation diagram in the $(|w|, \Gamma)$-plane, where w is the mid-height, mid-gap axial velocity. For the side-panels, the aspect-ratio Γ was changed in steps of $\Delta\Gamma = 0.001$ (after every 10^6 time steps), resulting in a ramp rate of $d\Gamma/dt = 10^{-4}$, see the text for details, and the grid-size is 21×21.

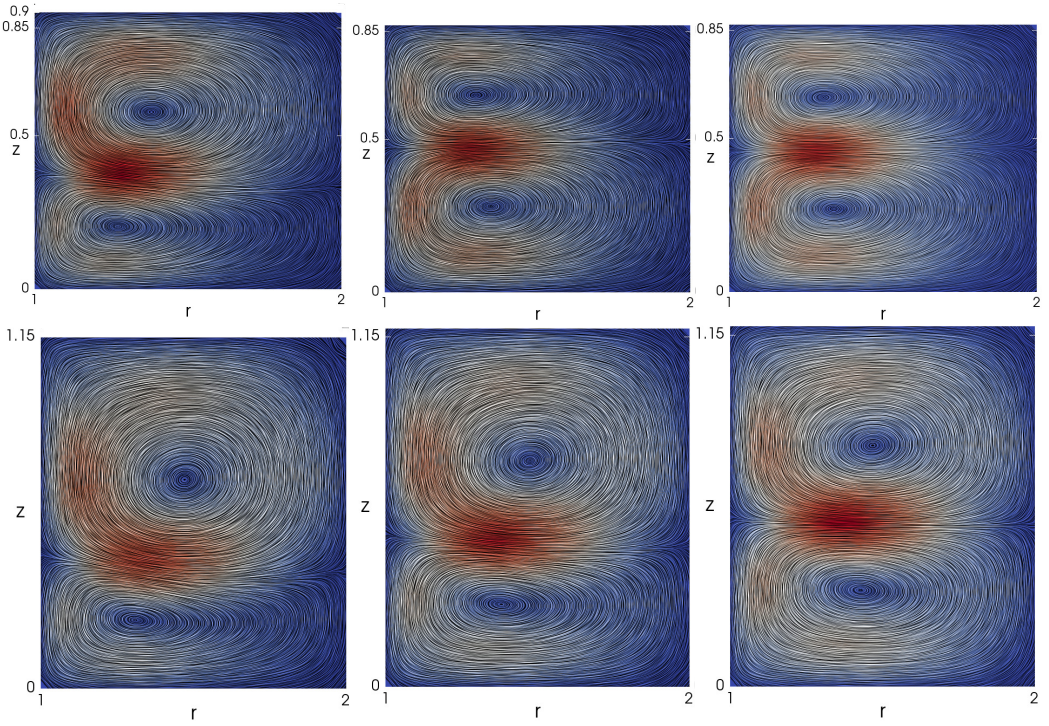

FIGURE S.25. Top row: streamline plots on the meridional (r, z)-plane for $\Gamma = 0.9$, 0.87 and 0.867 (from left to right), corresponding to the 1-roll branch on the left panel of figure S.24. Bottom row: streamline plots on the meridional (r, z)-plane for $\Gamma = 1.15$, 1.18 and 1.182 (from left to right), corresponding to the 1-roll branch on the right panel of figure S.24.

Appendix B. Asymmetric two-rolls and the effect of ramping rate on subcritical/hysteretic transitions

The phase-diagram in figure 16(a) in the main paper (Aghor & Alam 2021) was constructed largely using the 'Γ-increase/decrease' protocol, with a ramp rate of $d\Gamma/dt = 2.5 \times 10^{-4}$, which indicated that '$2 \to 1$'-transition is sub-critical at $\Gamma < 1$ as confirmed in the bifurcation diagrams in figure 17(a-e) in Aghor & Alam (2021). A few data points in figure 16(a), marked by filled circles and squares, were obtained using the 'Re-increase/decrease' protocol (such as in figure 15(d); Aghor & Alam (2021)). In the context of the present "transient" DNS code, a pertinent question: did we track the bifurcation points accurately with a finite ramping rate? Since the relaxation time diverges at the bifurcation point, the ramping rate should be as small as possible.

To ascertain the possible effects of ramp rate on the sub-critical transition over the range of studied Γ in figure 16(a), we have reconstructed figure 17(a), that holds for $Re = 180$, with a slower ramp rate, see figure S.24. In particular, to identify the left hysteresis-loop, the simulations were started from the 1-roll branch by decreasing aspect-ratio from $\Gamma = 0.9$ in steps of $\Delta\Gamma = 0.001$ after every 10^6 time steps – this corresponds to a ramp rate of $d\Gamma/dt = 10^{-4}$ and subsequently the simulations were restarted from the 2-roll branch at $\Gamma = 0.85$ by increasing Γ in steps of $\Delta\Gamma = 0.001$ after every 10^6 time steps at the same ramp rate. The same protocol was used to identify the right hysteresis-loop by starting simulations from $\Gamma = 1.15$. The related bifurcation diagrams in the $(|w|, \Gamma)$-plane are shown on the left and right panels of figure S.24, with its center panel being the original figure 17(a) of Aghor & Alam (2021).

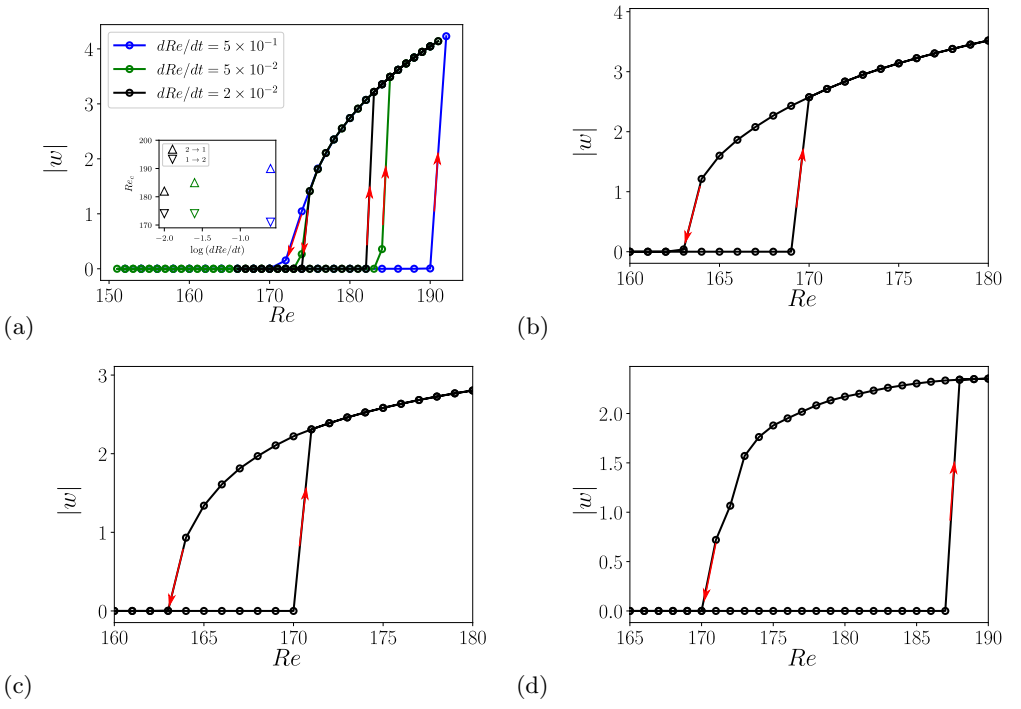

FIGURE S.26. (a) Effect of ramp-rate on the bifurcation diagram in the $(Re, |w|)$-plane at an aspect ratio of $\Gamma = 0.9$. Inset shows the variation of the Reynolds number for the bifurcation point (triangles) and limit points (inverted triangles) with ramp-rate. (b,c,d) Persistence of subcritical bifurcations at (b) $\Gamma = 1.0$, (c) $\Gamma = 1.1$ and (d) $\Gamma = 1.15$; the ramp-rate in panels (b-d) is set to $dRe/dt = 0.02$.

It is clear from figure S.24 that the locations of both limit points ($\Gamma_L^{LP} \approx 0.867$ and $\Gamma_R^{LP} \approx 1.182$) remained nearly fixed with $d\Gamma/dt = 10^{-4}$ (left and right panels) and $d\Gamma/dt = 2.5\times10^{-4}$ (centre panel), but the bifurcation points (Γ_L^{BP} and Γ_R^{BP}) have moved slightly closer to the respective limit point with a decreased ramping rate. Consequently, the range of Γ over which hysteresis occurs has decreased with decreasing ramping rate. However, the point to be noted is that both hysteresis loops survive ($\Gamma_L^{BP} - \Gamma_L^{LP} > 0$ and $\Gamma_R^{LP} - \Gamma_R^{BP} > 0$) even at the lowest ramping rate considered. With reference to figure 17(a) of Aghor & Alam (2021), it should be noted that the bifurcation and limit points at $Re = 180$ correspond to a ramp rate of $d\Gamma/dt = 10^{-4}$ (as in the left and right panels of figure S.24), while the remaining data points (open symbols) have been obtained with a larger ramp-rate of $d\Gamma/dt = 2.5 \times 10^{-4}$.

Figure S.25 displays the streamline plots for asymmetric rolls belonging to the left (top row) and right (bottom row) hysteresis loops (viz. figure S.24) at various values of the aspect ratio Γ. It is seen that, for both cases, the asymmetric rolls gradually transform towards a symmetric 2-roll state with (de/in)creasing Γ on the left and right hysteresis loops, respectively.

To further verify the robustness of observed subcritical bifurcation in figure 16(a), we have carried out ramping-simulations with Re-increase/decrease protocol by employing the homotopy technique (i.e. the asymmetric axial boundary condition on the temperature, Eq. (4.1)), see the discussion in §4.1 of the main paper (Aghor & Alam 2021). The bifurcation diagrams in the $(Re, |w|)$-plane are displayed in figures S.26(a–d) at

$\Gamma = 0.9, 1.0, 1.1$ and 1.15, respectively. For all Γ the bifurcation is found be sub-critical, reconfirming that the persistence of the left and right hysteresis loops in figure 16(a) (main paper) for the case of compressible TCF ($Ma = 1$). The inset of figure S.26(a) indicates that the limit-point Reynolds number (Re^{LP}, marked by inverted triangles in the inset) is accurately captured if a ramp rate of $dRe/dt = 5 \times 10^{-2}$ is used ($Re^{LP} = 174$ at $dRe/dt \leqslant 5 \times 10^{-2}$); on the other hand, the location of the bifurcation point (Re^{BP}, marked by the triangles in the inset) is nearly invariant at a ramp rate of $dRe/dt = 2 \times 10^{-2}$. That the limit and bifurcation points ($Re^{BP} \approx 180 > Re^{LP} = 174$) remain separated has been confirmed by extrapolating Re^{BP} and Re^{LP} at the zero ramp-rate using the Richardson extrapolation technique on the data set for three ramping rates ($dRe/dt = 0.5, 0.05$ and 0.02).

Collectively, from the above analysis, we conclude that the '$2 \rightarrow 1$'-roll transition is indeed sub-critical in compressible Taylor-Couette flow over a broad range of aspect-ratios around $\Gamma = 1$. This finding is in contrast to the super-critical nature of '$2 \rightarrow 1$'-roll transition in incompressible TCF for aspect-ratios $\Gamma < 1.23$, except over a very narrow range of $1.23 \leqslant \Gamma \leqslant 1.26$ where the transition is sub-critical and the disconnected solutions appear at $\Gamma > 1.26$; see figure 16(b) in the main paper (Aghor & Alam 2021). We have also demonstrated in figure 17(c-d) (Aghor & Alam 2021) that the range of Γ over which the above bistability occurs increases with increasing Mach number for a given Reynolds number. Therefore, we conclude that the gas-compressibility makes the '$2 \rightarrow 1$'-roll transition sub-critical in compressible Taylor-Couette flow.

REFERENCES

Aghor, P. & Alam, M. 2021 Nonlinear axisymmetric Taylor-Couette flow in a dilute gas: multi-roll transition and the role of compressibility. *J. Fluid Mech.*, **90?**, A?? (In press)

Harada, I. 1980 Computation of strongly compressible rotating flows. *J. Comp. Phys.*, **38**, 335-356.

Hyun, J. M. & Park, J. M. 1992 Spin-up from rest of a compressible fluid in a rapidly rotating cylinder. *J. Fluid Mech.*, **237**, 413-434.

LeVeque, R. J. 2007 *Finite Difference Methods for Ordinary and Partial Differential Equations*, SIAM Publishers. Philadelphia.